



## Dynamic compressive response of composite square honeycombs

S. Park, B.P. Russell\*, V.S. Deshpande, N.A. Fleck

Department of Engineering, Cambridge University, Trumpington Street, Cambridge CB2 1PZ, UK

### ARTICLE INFO

#### Article history:

Received 12 October 2011  
Received in revised form 18 November 2011  
Accepted 29 November 2011  
Available online 7 December 2011

#### Keywords:

A. Honeycomb  
A. Carbon fibre  
B. Impact behaviour  
E. Joints/joining

### ABSTRACT

Carbon fibre–epoxy composite square honeycombs, and the parent composite material, were tested in quasi-static compression at a strain rate of  $10^{-3}$  s $^{-1}$  and in dynamic compression at strain rates of  $10^3$ – $10^4$  s $^{-1}$  using an instrumented Kolsky bar arrangement. Taken together, these tests provide an assessment of the potential of this composite topology for use as a lightweight sandwich core. The honeycombs had two relative densities, 0.12 and 0.24, and two material orientations,  $\pm 45^\circ$  and  $0/90^\circ$  with respect to the prismatic, loading direction of the honeycomb. Honeycomb manufacture was by slotting, assembling and bonding together carbon fibre/epoxy woven plies of composite sheets of  $2 \times 2$  twill weave construction. The peak value of wall stress in the honeycombs was about one third that of the parent material, for all strain rates. An elastic finite element analysis was used to trace the source of this knock-down in strength: a stress concentration exists at the root of the slots and leads to premature failure by microbuckling. Shock-wave effects were evident at impact velocities exceeding 50 ms $^{-1}$  for the honeycomb of relative density 0.12. This was traced to stubbing of the buckled cell walls against the face of the Kolsky bar.

© 2011 Elsevier Ltd. All rights reserved.

### 1. Introduction

Long fibre polymer matrix composites are finding increasing application as load-bearing components in aircraft, and in lightweight armour design, due to their superior stiffness and strength to density ratios compared with traditional materials such as aluminium, steel and titanium alloys. These composites also show promise for low density cores in sandwich construction. But, in order to use these materials in a sandwich topology, it is necessary to characterise their static and dynamic responses, including operative failure mechanisms.

There is a growing body of experimental studies on the high strain rate compressive response of composites made from carbon or glass fibres and an epoxy matrix [1–4]. In broad terms, mild strain rate sensitivity is observed as the strain rate is increased from  $10^{-3}$  s $^{-1}$  to  $10^3$  s $^{-1}$ , with the peak strength doubling over this range. The consensus is that failure is dictated by fibre microbuckling and the strain rate sensitivity is associated with that of the matrix. At very high strain rates, above  $10^4$  s $^{-1}$ , micro-inertia effects are anticipated such that the micro-inertia of the fibres stabilise them against microbuckling (Slaughter and Fleck [5]).

Recently, a variety of composite lattices cores have been fabricated and their performance evaluated under quasi-static loading. For example, Finnegan et al. [6] have constructed pyramidal truss core sandwich panels by assembling and bonding water-jet cut

struts from  $0/90^\circ$  carbon fibre laminate sheets. They demonstrated the superior strength-to-density ratio of the composite compared to the equivalent aluminium lattices. However, the composite cores did not attain their full potential due to premature failure of the joints. Kazemahvazi et al. [7] constructed corrugated composite sandwich structures with unidirectional carbon fibre laminate using a moulding technique and measured their out-of-plane compressive and transverse shear responses. Two types of structure were manufactured: one with monolithic corrugations, and the other with foam-cored sandwich corrugations. They benchmarked the stiffness and strength of the composites against those of commercially available aluminium honeycomb and Nomex honeycomb. Kazemahvazi et al. [7] found that the carbon fibre composite construction, particularly in the sandwich configuration, outperformed the two commercial cores by up to an order of magnitude on an equal mass basis. Likewise, Russell et al. [8] found that composite sandwich panels with a honeycomb core had superior out-of-plane compressive and shear strengths to the equivalent metallic panel, on an equal mass basis. They manufactured the composite square honeycombs by slotting, assembling and bonding together carbon fibre/epoxy woven-plies, of orientation  $\pm 45^\circ$  and  $0/90^\circ$  with respect to the loading direction.

There is a recent literature on the dynamic compressive response of sandwich cores, using the direct-impact Kolsky bar test [9–11]. For example, Radford et al. [9] have measured the dynamic compressive response of stainless-steel square honeycombs and have identified sources of dynamic strength enhancement of these honeycomb cores. They concluded that the square honeycomb core

\* Corresponding author. Tel.: +44 1223748541.

E-mail address: [bpr23@eng.cam.ac.uk](mailto:bpr23@eng.cam.ac.uk) (B.P. Russell).

is a promising geometry for sandwich panels under shock loading. Numerical analyses of sandwich panels containing a honeycomb core and subjected to water-blast loading support this finding [12,13].

The aim of the present paper is to explore the dynamic response of carbon fibre – epoxy honeycomb cores for sandwich panel application. The cores are made from a  $2 \times 2$  twill weave of Toray T300-6 k carbon fibres in Fiberite 934 epoxy, and are of orientation  $\pm 45^\circ$  and  $0/90^\circ$  with respect to the loading direction. The degree to which the compressive strength is elevated by material strain rate effects and by micro-inertial effects is explored. As a baseline reference, the uniaxial compressive response of the parent wall material is measured over a wide range of strain rate. High speed photography is used to capture the deformation history.

## 2. Specimen manufacture

Two types of specimen were manufactured from the woven Toray T300 carbon fibre in Hexcel, type 934 epoxy: (i) single-ply walled square honeycombs specimens, and (ii) a 28-ply laminate for baseline materials tests. The manufacture of each type of specimen is described in turn.

### 2.1. Square honeycomb construction

The procedure for making composite square honeycombs follows that of Russell et al. [8]. Single ply sheets of the  $2 \times 2$  twill weave T300/934 composite were acquired from Carbon Technology<sup>1</sup> in the as-cured state. The curing cycle for the woven sheet material was as follows. Single sheets of a woven-ply were sandwiched between aluminium platens in order to achieve a smooth surface finish. The sandwiched sheets were vacuum bagged and autoclaved at  $180^\circ\text{C}$  and 7 bar for a period of 2 h.

Square honeycombs with a wall thickness  $t = 0.355$  mm (equal to that of a single ply), were constructed such that the ply fibre orientation (labelled 3 in Fig. 1) was  $\pm 45^\circ$  and  $0/90^\circ$  with respect to the prismatic direction of the honeycomb. The cell spacing  $L$  of the honeycomb was taken to be either 2.96 mm or 5.52 mm in order to generate honeycombs of relative density  $\bar{\rho} = 0.24$  and  $\bar{\rho} = 0.12$ , respectively. The overall in-plane size of the specimen was  $6 \times 6$  cells for  $\bar{\rho} = 0.24$  (see Fig. 1) and  $3 \times 3$  cells for  $\bar{\rho} = 0.12$ , in order to fit within the Kolsky bar apparatus.

To form complete cells, the in-plane width of the specimens was  $w = 3.7L$  for the  $3 \times 3$  cells and  $w = 6.8L$  for the  $6 \times 6$  cells, Fig. 1. The wall height  $H$  was chosen such that the aspect ratio was held constant at  $H/L = 3$  for all specimens. The cured woven ply was cut and slotted using a 2-axis micro-milling machine. The strips were assembled into a square honeycomb configuration (Fig. 1) and a low viscosity epoxy resin (Opti-tec 5001<sup>2</sup>) was applied to the joints. The whole assembly was then bonded at  $65^\circ\text{C}$  for 1 h. A slot width of  $s = 0.40$  mm was chosen to give sufficient tightness of the joint.

The geometry of the square honeycombs is summarised in Table 1. Throughout this paper, the geometry will be indicated by its relative density and by the weave orientation with respect to the prismatic direction of the honeycomb.

### 2.2. 28-ply laminate construction

In order to measure the in-plane uniaxial compressive response of  $\pm 45^\circ$  and  $0/90^\circ$  parent material, specimens were prepared of suf-

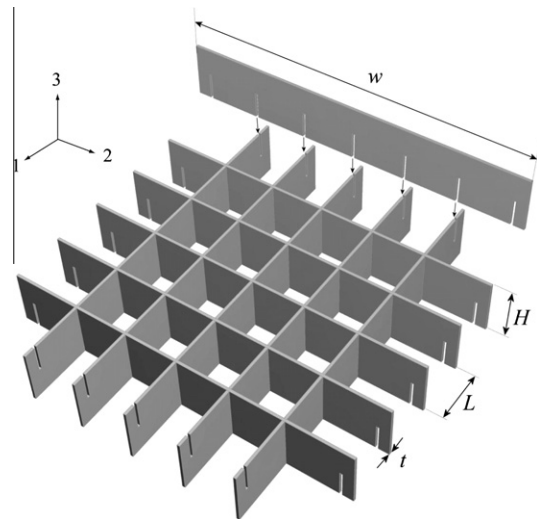


Fig. 1. Sketch illustrating the assembly of the  $6 \times 6$  honeycomb from slotted CFRP sheets.

Table 1

Critical dimensions of the specimen made from  $\pm 45^\circ$  and  $0/90^\circ$  honeycomb specimens.

$\bar{\rho}$	Weave orientation	Cells	$w$ (mm)	$H$ (mm)	$L$ (mm)	$t$ (mm)
0.12	$\pm 45^\circ$	$3 \times 3$	20.2	17.8	5.9	0.36
	$0/90^\circ$					
0.24	$\pm 45^\circ$	$6 \times 6$	20.2	8.9	3.0	0.36
	$0/90^\circ$					

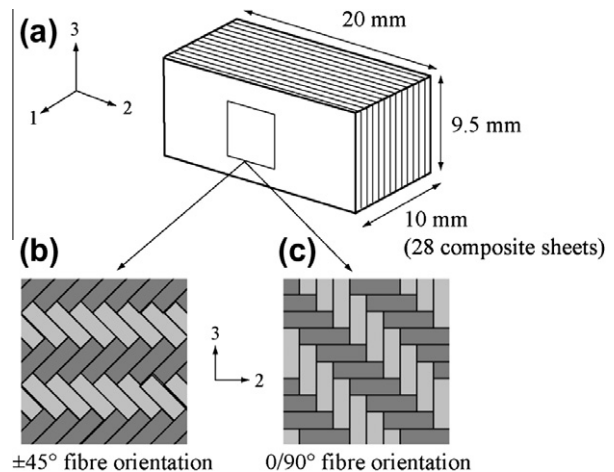


Fig. 2. (a) The 28-ply laminate, with plies arranged in the (b)  $\pm 45^\circ$  or (c)  $0/90^\circ$  configurations.

ficient stockiness to prevent macrobuckling. As-cured composite plies of T300/934 were cropped into rectangles measuring 20 mm by 10 mm, and 28 plies were bonded together using Opti-tec 5001 epoxy resin for 1 h at  $65^\circ\text{C}$  in order to form a “28-ply laminate” of thickness 10 mm. The volume fraction of resin was less than 1% and had a negligible effect upon specimen dimensions. Two types of specimens were constructed such that the fibre tows were orientated at  $\pm 45^\circ$  and  $0/90^\circ$  with respect to the loading direction, Fig. 2. The specimens were end-machined to give parallel ends and a specimen height of 9.5 mm.

<sup>1</sup> Carbon Technology, Ltd., Woodfield House, Woodfield Road, Altrincham Cheshire WA144ED, UK.

<sup>2</sup> Intertronics, 17 Station Field Industrial Estate, Banbury Road, Kidlington, Oxfordshire, OX51JD, UK.

### 3. Quasi-static experimental investigation

#### 3.1. Parent material properties

The compressive response of the 28-ply laminate specimens was measured at  $\dot{\epsilon} = 10^{-3} \text{ s}^{-1}$  by compressing the specimens along the 3-direction, as defined in Fig. 2. To achieve this, the specimens were end-loaded between the lubricated platens of a screw-driven test machine. Friction was minimised through use of PTFE sheets between specimen and platens. The nominal stress was inferred from the load cell of test machine and the true axial strain was measured directly by a strain gauge bonded on the specimen surface.

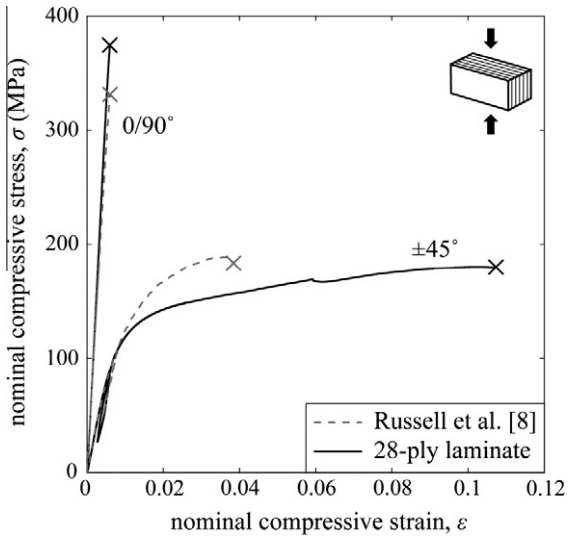


Fig. 3. The measured quasi-static compressive stress  $\sigma$  versus strain  $\epsilon$  response of the “28-ply laminate”.

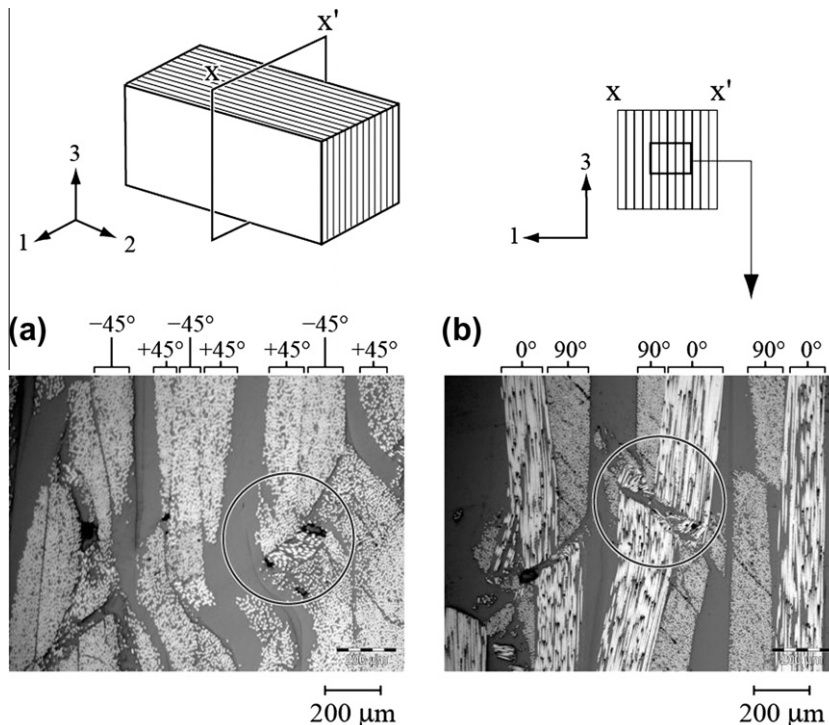


Fig. 4. Optical micrographs of the section X–X’ of the 28-ply laminate, for (a)  $\pm 45^\circ$  and (b)  $0/90^\circ$  configurations. The images were taken after the 28-ply laminate had been strained to 11% and 0.6% and then unloaded, for the  $\pm 45^\circ$  and  $0/90^\circ$  configurations, respectively. A microbuckled zone is shown by the encircled region on each micrograph.

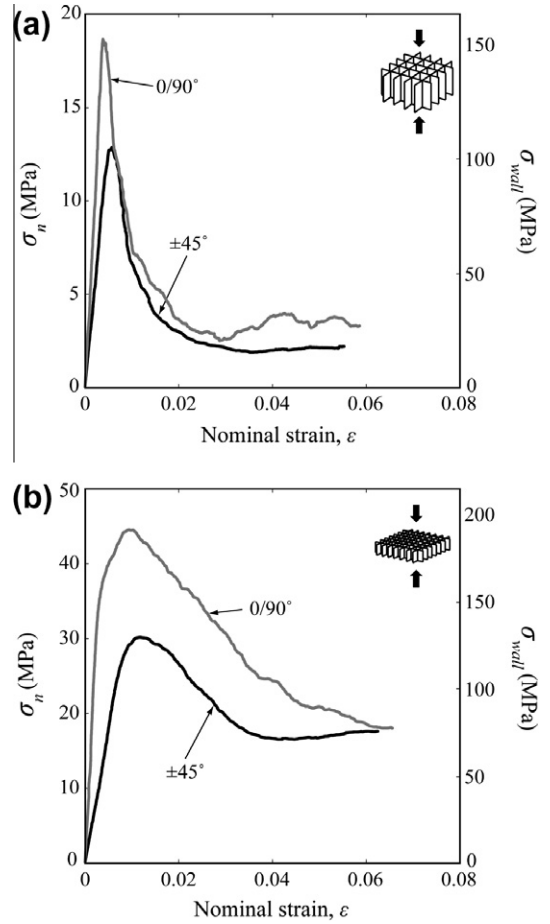


Fig. 5. Quasi-static compressive stress versus strain response for honeycombs of relative density (a)  $\bar{\rho} = 0.12$  and (b)  $\bar{\rho} = 0.24$ . Results are given in terms of nominal stress  $\sigma_n$  and wall stress  $\sigma_{wall}$ , for both ply orientations.

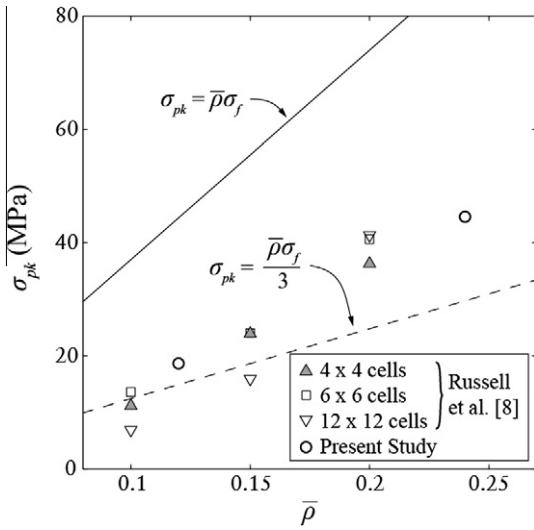


Fig. 6. The measured nominal peak stress as a function of the relative density  $\bar{\rho}$ . The measurements from Russell et al. [8] are included.

The measured uniaxial compressive response of the 28-ply laminate in the  $\pm 45^\circ$  and  $0/90^\circ$  orientations is shown in Fig. 3. The  $0/90^\circ$  woven laminate exhibits a linear elastic response, with an axial modulus of 63 GPa and a peak strength of  $\sigma_f = 370$  MPa. In contrast, the  $\pm 45^\circ$  laminate has a quasi-ductile characteristic, with an axial modulus of 16 GPa, a peak strength of  $\sigma_f = 180$  MPa and a failure strain of 9%. The previously measured compressive response of the same laminate (Russell et al. [8]) is included in Fig. 3 and is in excellent agreement with the current measurements.

The compressive failure mechanisms of the 28-ply laminate have been investigated by examining a transverse section using an optical microscope, see Fig. 4. The  $0/90^\circ$  28-ply laminate failed by plastic microbuckling of the load-bearing  $0^\circ$  tows, with the

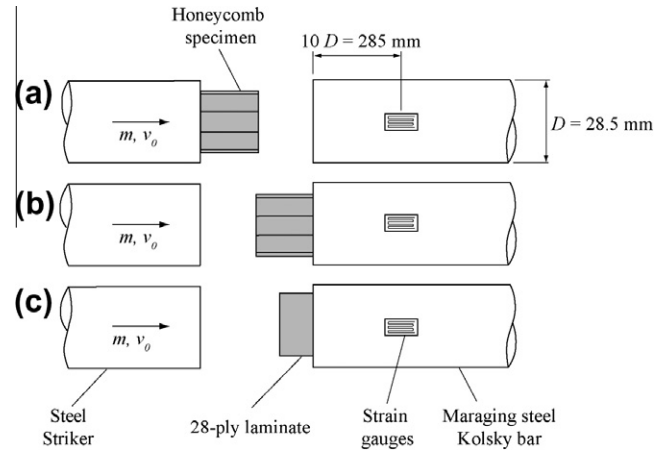


Fig. 8. Sketch of the set-up for the dynamic impact experiments, for (a) front face and (b) back face stress measurement of honeycombs, and (c) the back face configuration that was used to deduce the dynamic parent material properties from the 28-ply laminate.

characteristic snap-back instability at peak load, and at an axial strain of about 1%, see Fleck [14] for a review of this phenomenon. In contrast, the specimen with fibre orientations at  $\pm 45^\circ$  deformed by matrix shear with scissoring of the fibres. Ultimate fibre failure is again by plastic microbuckling, see Jelf and Fleck [15].

### 3.2. Response of the square honeycomb

Square honeycomb specimens were compressed along the prismatic direction using the same test arrangement as for the 28-ply laminate. Again, a strain rate of  $\dot{\epsilon} = 10^{-3} \text{ s}^{-1}$  was employed, but now the axial strain was deduced via a laser extensometer using a gauge length equal to the specimen height.

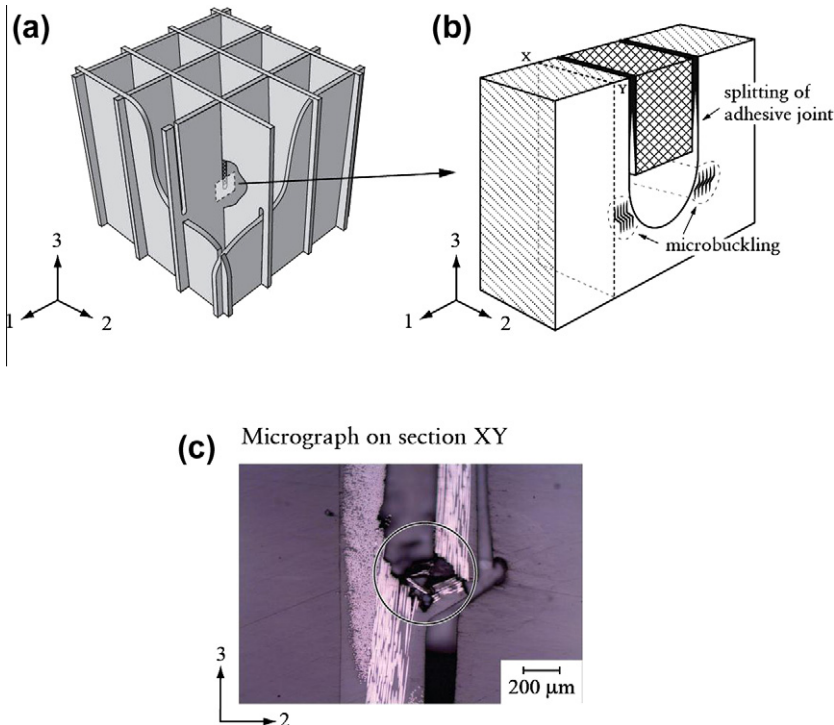
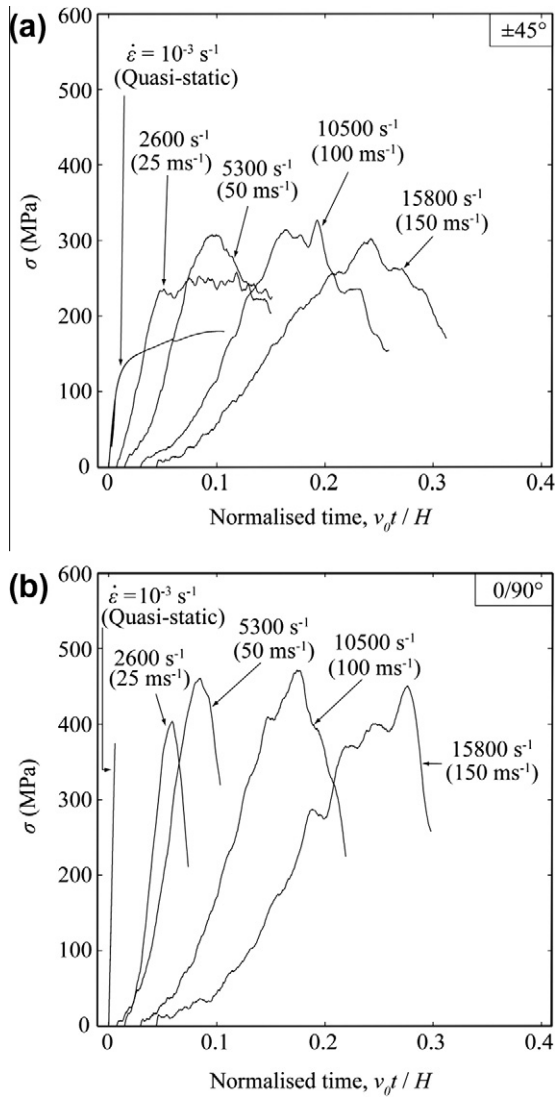


Fig. 7. (a) Sketch of a  $3 \times 3$  cell honeycomb with cut-a-way to reveal details of the slot. (b) A magnified view of the slot end, showing debonding of the adhesive joint, that precedes microbuckling around the slot end. (c) An optical micrograph of the  $\bar{\rho} = 0.12$ ,  $0/09^\circ$  honeycomb deformed to a strain  $\epsilon = 0.04$  and then unloaded. The micrograph shows the slot root on section  $X$ – $Y$  as defined in (b). A microbuckled zone is shown by the encircled region on the micrograph. (For interpretation of the references to colour in this figure legend, the reader is referred to the web version of this article.)



**Fig. 9.** Stress versus normalised time measurements in the (a)  $\pm 45^\circ$  and (b)  $0/90^\circ$  28-ply laminate specimens for four impact velocities. For the dynamic tests the curves are labelled by both the applied strain rate ( $v_0/H$ ) and the corresponding impact velocities  $v_0$ .

The compressive stress–strain responses of the honeycombs are plotted in Fig. 5; both the compressive stress on the nominal cross-section of the specimen  $\sigma_n$  and the wall stress  $\sigma_{wall} = \sigma_n/\bar{\rho}$  are included. Following an initial linear response, a peak strength is observed, followed by a progressive drop in stress until a plateau value is attained. The peak wall stress  $\sigma_{wall}$  is highest for the specimen of orientation  $0/90^\circ$  and relative density  $\bar{\rho} = 0.24$ . In all cases the peak wall stress is less than half that of the parent material, recall Fig. 3.

The peak nominal stress  $\sigma_{pk}$  of the  $0/90^\circ$  honeycomb is plotted as a function of  $\bar{\rho}$  in Fig. 6, along with previous data taken from Russell et al. [8] for  $0/90^\circ$  honeycomb cores adhered to steel face-sheets. Recall that the current tests on free-standing honeycomb core comprise  $3 \times 3$  cells for  $\bar{\rho} = 0.12$  and  $6 \times 6$  cells for  $\bar{\rho} = 0.24$ . The number of cells was varied systematically in Russell et al. [8] and it was demonstrated therein that the peak strength is almost insensitive to the number of cells.

The current data are in good agreement with those of Russell et al. [8], implying that the degree of adherence to facesheets has a negligible effect upon the compressive strength. It is instructive to compare the measured nominal peak stress  $\sigma_{pk}$  of the honeycomb with

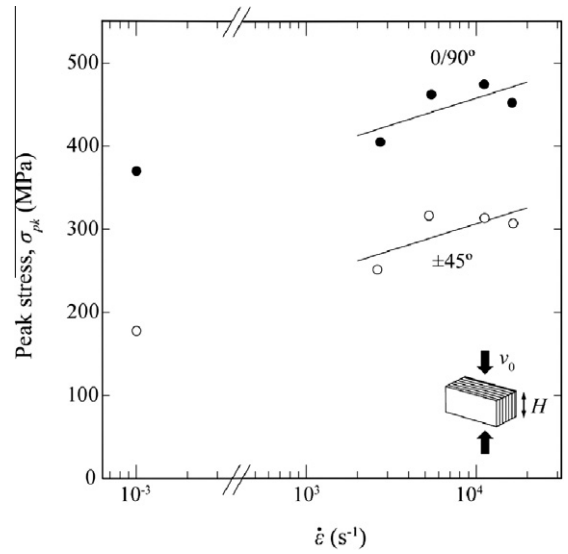


**Fig. 10.** The measured peak strength  $\sigma_{pk}$  of the parent material as a function of the applied strain rate  $\dot{\epsilon} = v_0/H$ .

the compressive failure strength  $\sigma_f$  of the parent material. Absent any stress concentrations and intervening failure mechanisms (such as macro-buckling), we would anticipate a failure locus of  $\sigma_{pk} = \bar{\rho}\sigma_f$ , as sketched in Fig. 6. However, the measured peak strength of the honeycomb  $\sigma_{pk}$  is about one third of this prediction, as indicated by the trajectory  $\sigma_{pk} = \bar{\rho}\sigma_f/3$  in Fig. 6. We shall argue below that the knock-down factor is due to a stress concentration at the root of the slots in the sheets of the honeycomb.

### 3.3. The observed failure mechanism

In order to investigate the failure sequence, tests were interrupted beyond the peak load at a compressive nominal strain of 4%, and the specimen was then visually examined. The local failure mechanisms were confirmed by sectioning, polishing and by examination in an optical microscope.

Debonding along the bonded slots from the slot-ends was observed early in the test (at less than 50% of the peak load) and this is a consequence of the relatively weak and brittle adhesive. The debonding event decouples the mating orthogonal sheets of the honeycomb and increases the stress concentration at the ends of the slots. This stress concentration is analysed in Appendix A via a finite element study. An orthotropic, elastic analysis is conducted in order to assess the level of stress concentration at the root of the honeycomb slots, with a view to estimate the onset of damage in the composite (not final failure).<sup>3</sup>

It is shown that the stress concentration factor  $\kappa_T$  at the root of the slot is approximately 2.8 for the  $\pm 45^\circ$  lay-up and 2.9 for the  $0/90^\circ$  lay-up. This local stress concentration triggers fibre microbuckling from the root of the slot. Optical microscopy confirmed this failure mechanism, as shown for the  $\bar{\rho} = 0.12$ , and  $0/90^\circ$  honeycomb in Fig. 7. Initiation of the microbuckling event occurs at peak load. Thus, we anticipate that  $\sigma_{pk}$  is given by

$$\sigma_{pk} = \bar{\rho}\sigma_f/\kappa_T$$

This prediction is in good agreement with the data shown in Fig. 6; the observed knock-down factor of 3 is close to the value of stress concentration factor,  $\kappa_T$ .

<sup>3</sup> It is appreciated that a much more sophisticated analysis is needed to model the progression of a number of failure processes.

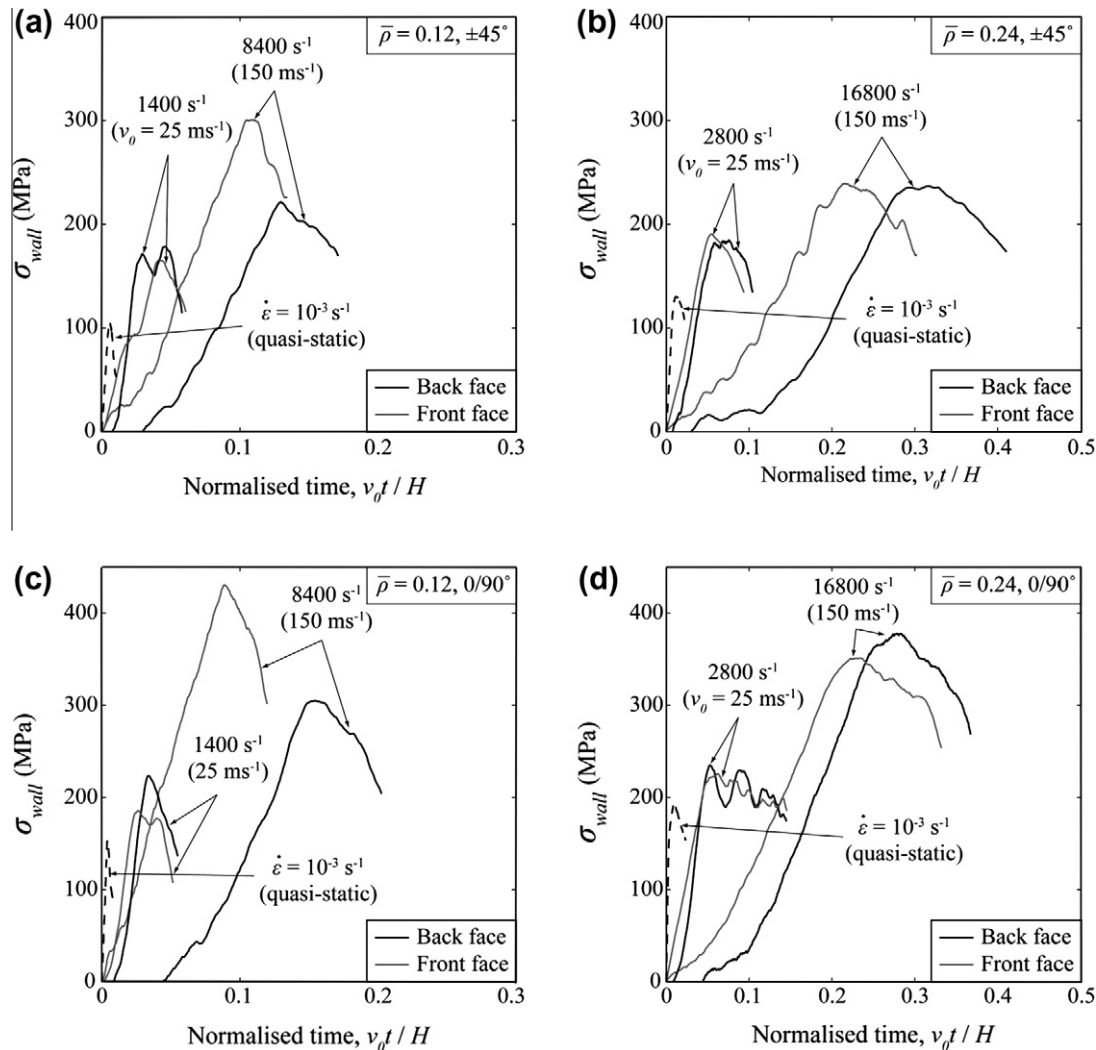


**Fig. 11.** The measured walls stress  $\sigma_{wall}$  versus the normalised time  $v_0 t / H$  curves for strain rates  $\dot{\epsilon} = v_0 / H$  in the range  $10^{-3} \text{ s}^{-1}$ – $1.68 \times 10^4 \text{ s}^{-1}$  (the corresponding impact velocities  $v_0$  are shown in brackets). The  $\pm 45^\circ$  honeycombs are marked in (a) and (b) for  $\bar{\rho} = 0.12$  and  $\bar{\rho} = 0.24$ , respectively while (c) and (d) present results for the  $\bar{\rho} = 0.12$  and  $\bar{\rho} = 0.24$   $0/90^\circ$  honeycombs, respectively.

## 4. Dynamic investigation

### 4.1. Dynamic test setup

The dynamic experimental setup follows closely that developed by Radford et al. [9]. A gas-gun with a barrel length of 4.5 m and a bore of 28.5 mm was used to accelerate low carbon steel striking bars with masses between  $M = 0.09$  kg and 2.4 kg at velocities from  $v_0 = 25$  to  $200 \text{ m s}^{-1}$ . An instrumented Kolsky bar, positioned at the distal end of the specimen with respect to the striker bar, was used to infer the load during the impact event.

The maraging steel (M-300) Kolsky bar of length 2.2 m and diameter 28.5 mm, was instrumented by two 1 mm strain gauges mounted diametrically opposite each other at a distance of 10 diameters from the impact end. The strain gauges were wired in the half-Wheatstone bridge configuration, and the signal recorded on a digital oscilloscope via an amplifier with a cut-off frequency of 500 kHz. The force transmitted to the Kolsky bar from the test specimens was inferred from the strain measurement.

The striker mass was selected such that the kinetic energy of the projectile was much larger than the energy absorbed through deformation of the specimens, so to ensure a constant crush velocity. A large mass  $M$  was used at lower velocities ( $M = 2.4$  kg where

$v_0 \leq 35 \text{ m s}^{-1}$ ), and a small mass for higher velocities ( $M = 0.09$  kg where  $v_0 \geq 80 \text{ m s}^{-1}$ ). For all intermediate velocities we took  $M = 0.5$  kg.

The honeycomb specimens were impacted on the front face, and two test configurations were used to measure the compressive stress transient on the front face, or back, ‘distal’ face, see Fig. 8. In the front face configuration, the back face of the specimen was adhered (with double-sided tape) to the striker bar, as shown in Fig. 8a; the front face impacted the instrumented Kolsky bar and the force on the front face was thereby measured. In contrast, in the back face configuration, the back face of the specimen was adhered to the instrumented Kolsky bar, and the front face was impacted by the striker bar, as show in Fig. 8b. Additional tests on the 28-ply laminate were performed in order to measure the high strain rate response of the parent material in the back face configuration, see Fig. 8c.

### 4.2. Parent material strain-rate sensitivity

High strain rate compression experiments were performed on the 28-ply laminate at strain rates in the range of 2500–16,000  $\text{s}^{-1}$ , corresponding to impact velocities of 25–150  $\text{ms}^{-1}$ . Results for the material test specimens (28-ply laminates) with fibres oriented at  $\pm 45^\circ$  and  $0/90^\circ$  are shown in Fig. 9. Here, stress is

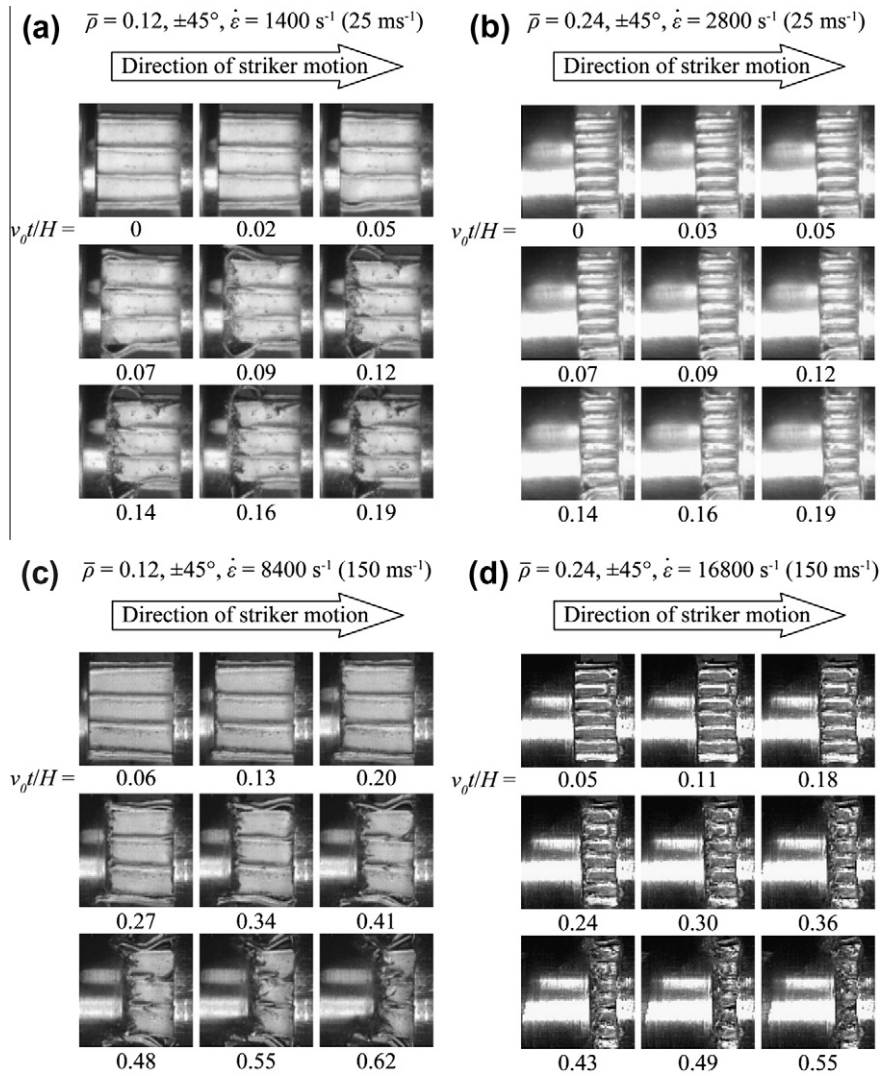


Fig. 12. Montage of high speed photographs showing the deformation of the  $\pm 45^\circ$  honeycombs impacted at  $25 \text{ m s}^{-1}$  (a and b) and  $150 \text{ m s}^{-1}$  (c and d). The  $\bar{\rho} = 0.12$  honeycombs are shown in (a) and (c) while the  $\bar{\rho} = 0.24$  honeycombs are given in (b) and (d).

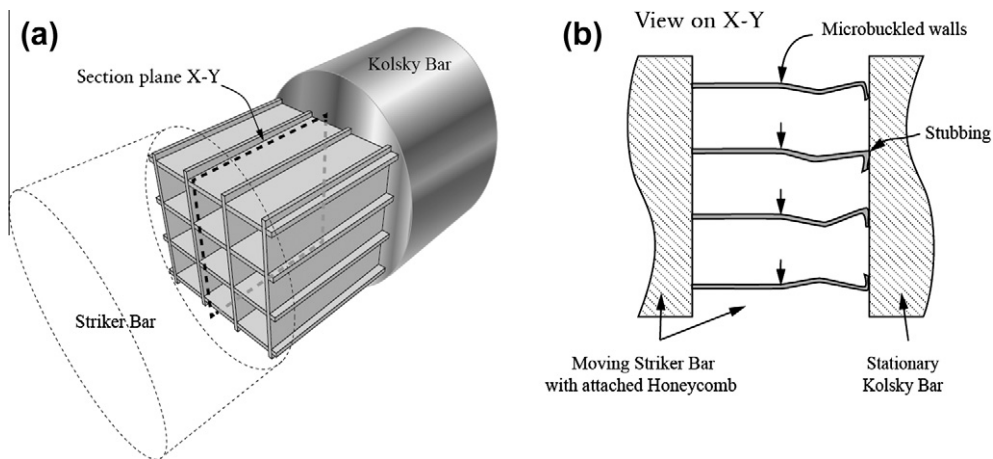
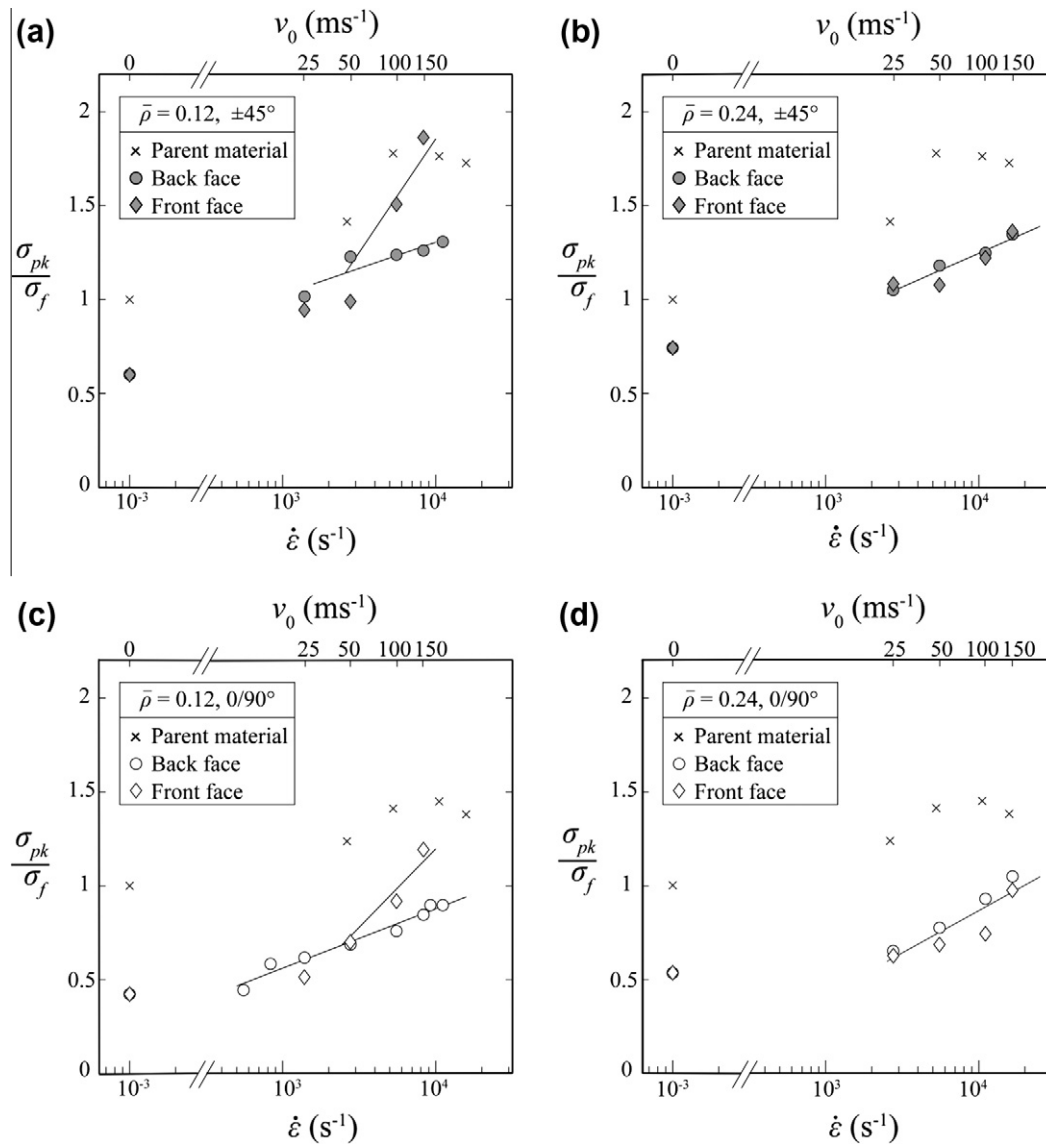


Fig. 13. (a) Illustration of the  $3 \times 3$  cell honeycomb at the point of impact in the front face configuration (the striker bar is shown in dashed-outline for clarity). (b) A sketch of the cross-section X-Y illustrating the buckling and stubbing of the honeycomb cell walls against the stationary Kolsky bar.

plotted against non-dimensionalised time,  $v_0 t/H$ , where  $v_0$  is the impact velocity,  $t$  is the elapsed time from the instant of impact of the striker on the specimen and  $H = 9.5 \text{ mm}$  is the height of the

specimen, see Fig. 2. The stress in the specimen is taken to be the measured force inferred from the Kolsky bar arrangement over the cross-sectional area of the specimen.



**Fig. 14.** The measured peak wall stress  $\sigma_{pk}$  normalised by the static peak strength  $\sigma_f$  of the parent material as a function of the inferred strain rate. The corresponding impact velocities  $v_0$  for the honeycombs are labelled on the upper x-axis. Measurements are shown for the  $\pm 45^\circ$  honeycomb with (a)  $\bar{\rho} = 0.12$  and (b)  $\bar{\rho} = 0.24$ , and for the  $0/90^\circ$  honeycomb with (c)  $\bar{\rho} = 0.12$  and (d)  $\bar{\rho} = 0.24$ .

Some care is required in the interpretation of Fig. 9. The stress history is increasingly influenced by elastic wave propagation effects as the impact velocity increases. Consider the most extreme case, for which  $\dot{\epsilon} = 16,000 \text{ s}^{-1}$  and  $v_0 = 150 \text{ ms}^{-1}$ . The elastic wave reaches the rear face of the specimen after a time  $t = H/c_0$  where  $c_0 \approx 5000 \text{ ms}^{-1}$  is the elastic wave propagation speed. Upon recalling that the specimen height  $H$  equals 9.5 mm, we obtain  $t \approx 2 \mu\text{s}$ , and hence  $v_0/H = 0.03$  in this case. However, peak stress is attained at  $v_0t/H = 0.25\text{--}0.3$ , corresponding to 8–10 elastic wave reflections. We conclude that the peak stresses exhibited in Fig. 9 for both orientations occur after axial equilibrium has been established and hence can be considered to be a material property. In contrast, the measured nominal strains  $v_0t/H$  at peak load are amplified by wave propagation effects early in the test and hence do not represent a material property. The dependence of the measured peak stress  $\sigma_{pk}$  upon the imposed strain rate  $\dot{\epsilon}$  is summarised in Fig. 10, for both fibre orientations. Quasi-static data at  $\dot{\epsilon} = 10^{-3} \text{ s}^{-1}$  is included for comparison purposes. Both the  $0/90^\circ$  strength and the  $\pm 45^\circ$  strength increase by about 100 MPa as  $\dot{\epsilon}$  is increased from  $10^{-3} \text{ s}^{-1}$  to  $10^4 \text{ s}^{-1}$ . Failure is due to plastic microbuckling, and

the mild strain rate sensitivity of the composite is ascribed to that of the matrix. These measurements are largely consistent with those reported in the literature for the strain rate sensitivity of CFRP, see for example [1–4].

#### 4.3. High strain rate response of square honeycomb

The dependence of the compressive response of the  $0/90^\circ$  and  $\pm 45^\circ$  honeycombs upon strain rate is given in Fig. 11, for the  $\bar{\rho} = 0.12$  and  $\bar{\rho} = 0.24$ . First consider the  $\pm 45^\circ$  lay-up. The wall stress  $\sigma_{wall}$  on both the front and back faces of the specimen is plotted as a function of normalised time  $v_0t/H$  in Fig. 11a for  $\bar{\rho} = 0.12$ , and in Fig. 11b for  $\bar{\rho} = 0.24$ . The curves are labelled both by the imposed velocity  $v_0$  and the nominal strain rate  $v_0/H$ . Recall that  $v_0$  is varied from  $25 \text{ m s}^{-1}$  to  $200 \text{ m s}^{-1}$  for both values of relative density  $\bar{\rho}$ ; since the height  $H$  of  $\bar{\rho} = 0.12$  is twice that for  $\bar{\rho} = 0.24$ , the imposed strain rate  $\dot{\epsilon}$  also varies by a factor of two with relative density.

The sensitivity to strain rate is best explained by reference to the observed sequence of failure mechanisms. High speed photography (Fig. 12) and post-test examination revealed that the failure

sequence is independent of impact velocity. As for the quasi-static tests reported earlier in this study, peak load is set by microbuckle formation at the slot-roots of the honeycomb sheets. This microbuckle propagates across the net section of each cell, creating a bending hinge at mid-height. Subsequently, the cell walls stub against the striker face, see Figs. 12 and 13.

Now consider the collapse responses of Fig. 11a and b of the  $\pm 45^\circ$  honeycombs. At low impact velocities of  $v_0 \leq 25 \text{ m s}^{-1}$ , axial equilibrium is maintained and the front and back face stresses are almost equal. The peak stress is dictated by plastic microbuckling from the slot root, and increases with  $v_0$  due to the mild rate sensitivity of the parent material, as already discussed. Now consider the dynamic response at  $v_0 = 150 \text{ m s}^{-1}$ . A time lag is evident between the stress-time histories at the front and back faces due to the time taken for the elastic wave to propagate a distance  $H$  from the front to the back face. This time shift brings the front and back face responses into alignment for  $\bar{\rho} = 0.24$  see Fig. 11b. But additional effects are at play in the  $\bar{\rho} = 0.12$  case. The peak stress on the front face exceeds that on the back face by almost 100 MPa. This is ascribed to an inertial force on the stubbed cell wall, see Fig. 13. The measured force to bring this stubbed portion to rest (from the velocity  $v_0$ ) results in the high front face force measurement.

The high strain rate responses of the  $0/90^\circ$  honeycomb (Fig. 11c and d) are quantitatively similar to that of the  $\pm 45^\circ$  honeycomb – albeit the wall stresses are somewhat elevated – and the observed

collapse modes are the same. Hence, for the sake of brevity, the montage of the high speed photographs are omitted.

The measured peak wall stress  $\sigma_{pk}$  for each configuration of honeycomb has been normalised by the quasi-static compressive strength of the parent material  $\sigma_f$ , and  $\sigma_{pk}/\sigma_f$  is plotted as a function of  $\dot{\epsilon}$  (and  $v_0$ ) in Fig. 14. Both the front and back face values of  $\sigma_{pk}$  are displayed, and for completeness  $\sigma_{pk}$  for the parent material is included as a function of  $\dot{\epsilon}$ . Since the height  $H$  of the 28-ply parent laminate differs from that of the honeycombs, the  $v_0$  axis does not apply to the parent material data in Fig. 14.

The data shown in Fig. 14 support the above discussion, as follows:

- (i) For the range of  $v_0$  employed, shock effects (i.e. a higher front face stress than that of the back face) are negligible for both lay-ups of  $\bar{\rho} = 0.24$  honeycomb. However, shock effects are significant for  $v_0 \geq 50 \text{ m s}^{-1}$  in  $\bar{\rho} = 0.12$  honeycomb.
- (ii) The value of  $\sigma_{pk}$  on the back face of the honeycombs is half to one third that of the parent material, due to stress concentration at the root of the slot, as analysed in Appendix A for the quasi-static case.
- (iii) The peak back face stress  $\sigma_{pk}$  on the honeycomb increases with  $\dot{\epsilon}$  in line with that of the parent material due to the rate sensitivity of the matrix.

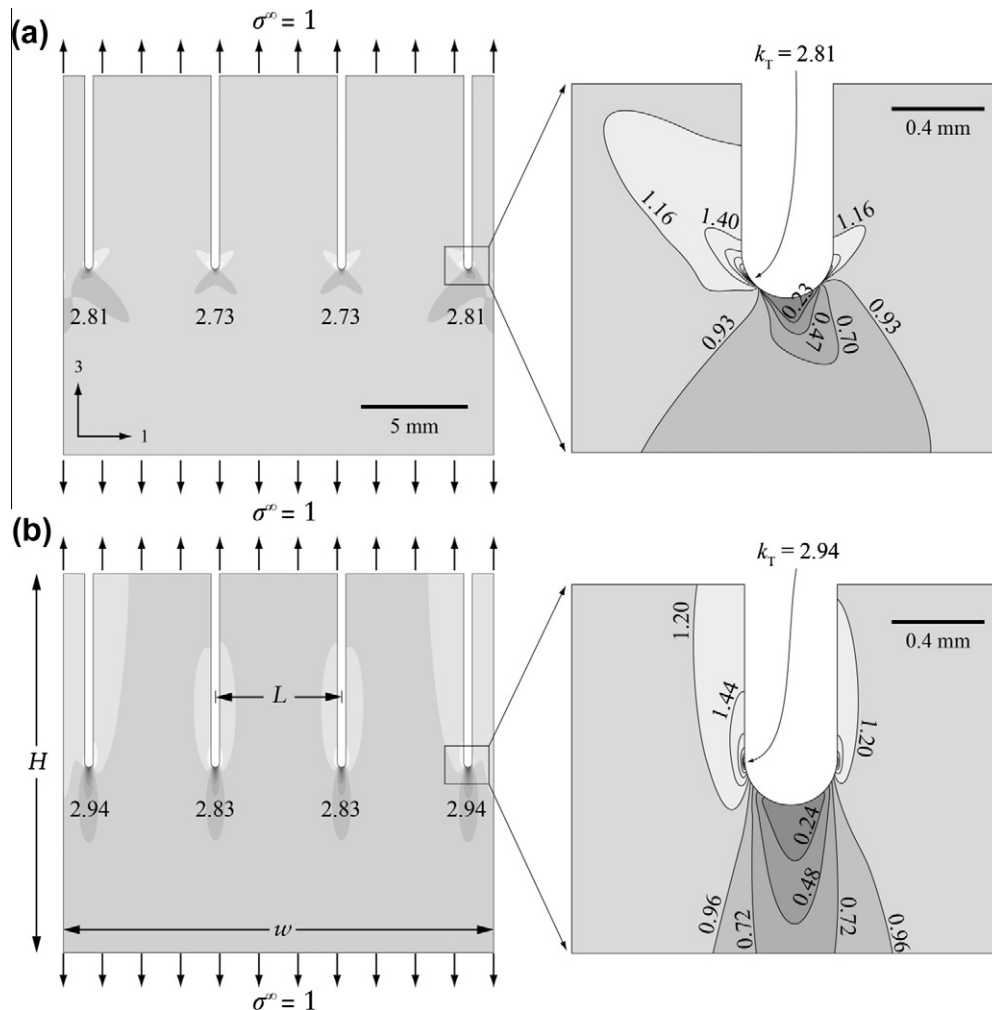


Fig. A1. FE predictions of the distribution of the maximum principal stress in a single slotted plate of the  $\bar{\rho} = 0.12$  honeycomb in the (a)  $\pm 45^\circ$  and (b)  $0/90^\circ$  configurations. The stress concentration factors  $k_T$  at the root of the slots are included.

**Table A1**

The orthotropic elastic properties used in the FE analysis.

Property	$\pm 45^\circ$ Orientation	0/90° Orientation
$E_1 = E_3$	16 GPa	63 GPa
$G_{13}$	27 GPa	4.7 GPa
$\nu_{13}$	0.70	0.16

- (iv) The normalised peak stress  $\sigma_{pk}/\sigma_f$  on the back face superpose for both values of  $\bar{\rho}$ . This indicates a common mechanism of failure.

## 5. Concluding remarks

The uniaxial compressive responses of CFRP square honeycombs of two relative densities and two fibre orientations have been measured over a wide range of strain rate, from  $10^{-3} \text{ s}^{-1}$  to  $10^4 \text{ s}^{-1}$ . In addition, the compressive response of the parent material has been determined.

Failure in all cases (parent material and honeycomb) was by plastic microbuckling and consequently, the observed strain rate sensitivity is ascribed to that of the matrix. The peak strength of the honeycombs is knocked down from the parent properties by a factor of about three which has been traced to the stress concentration factor at the slot-root of the honeycomb cell walls. Alternative manufacturing methods are required in order to reduce this stress concentration, and is left as a topic for future study.

In the high strain rate tests on honeycomb of  $\bar{\rho} = 0.12$ , shock-wave effects are evident at impact velocities exceeding  $50 \text{ m s}^{-1}$ . This is two orders of magnitude below the elastic wave speed for CFRP, and has been traced to stubbing of the buckled cell walls against the face of the Kolsky bar.

Fibre discontinuity at the slots ends fundamentally limits the strength of the honeycomb core discussed in this paper. Technologies such as 3D weaving [16] enable the fabrication of complex geometries whilst maintaining fibre continuity. Elimination of the stress concentration at the slot ends could lead to honeycombs with strength twice that achieved in this study.

## Acknowledgement

The authors are grateful for financial support from the Office of Naval Research under ONR Contract N00014-11-1-0650 (Dr. D. Shifler, Programme Manager).

## Appendix A. Finite element calculations of the stress concentration at the slot root

A small strain, plane stress orthotropic elastic analysis has been performed for the boundary value problem given in Fig. A1. This represents uniaxial tension of a single debonded sheet of the honeycomb. As this is a linear elastic analysis, tension and compression are equivalent differing only in sign. Thus tension has been used for convenience in the numerical simulations.

The geometry shown in Fig. A1 is for the  $\bar{\rho} = 0.12$  specimen, with height and width dimensions  $H = 17.8 \text{ mm}$  and  $w = 20.2 \text{ mm}$ ,

respectively. Slots of width  $s = 0.4 \text{ mm}$  are spaced at a distance  $L = 5.52 \text{ mm}$  and are of length  $R + H/2$ , where  $R = 0.2 \text{ mm}$  is the radius of the semi-circular end of the slot. The elastic properties of the  $\pm 45^\circ$  and 0/90° laminates are summarised in Table A1, using the global co-ordinate system as defined in Fig. 1 such that  $x_3$  is along the prismatic direction of the honeycomb. The composite was modelled using 4-noded plane stress elements with reduced integration, using ABAQUS Standard finite element code.

Contours of maximum principal stress  $\sigma_{\max}$  are shown in Fig. A1 for both fibre orientations, for an applied remote stress of  $\sigma^\infty = 1$ . The stress concentration factor  $k_T$  is defined on the basis of the largest value of  $\sigma_{\max}$ . This peak value occurs at the notch root, and the associated principal direction is aligned with the fibre direction for both the  $\pm 45^\circ$  and 0/90° orientations. We find that  $k_T = 2.8$  and 2.9 for  $\pm 45^\circ$  and 0/90° orientations, respectively, and is almost independent of the slot location across the width of the specimen, see Fig. A1. Additional calculations were performed for the  $\bar{\rho} = 0.24$  honeycomb:  $k_T$  remained approximately unchanged from the  $\bar{\rho} = 0.12$  case as  $L \gg R$  in both cases.

## References

- [1] Harding J. Effect of strain rate and specimen geometry on the compressive strength of woven glass-reinforced epoxy laminates. *Composites* 1993;24(4):323–32.
- [2] Hosur MV, Alexander J, Vaidya UK, Jeelani S. High strain rate compression response of carbon/epoxy laminate composites. *Comp Struct* 2001;52(3–4):405–17.
- [3] Gilat A, Goldberg RK, Roberts GD. Experimental study of strain-rate-dependent behavior of carbon/epoxy composite. *Comp Sci Technol* 2002;62(10–11):1469–76.
- [4] Bing Q, Sun CT. Modeling and testing strain rate-dependent compressive strength of carbon/epoxy composites. *Comp Sci Technol* 2005;65(15–16):2481–91.
- [5] Slaughter WS, Fleck NA. Microbuckling of fibre composites with random initial fibre waviness. *J Mech Phys Solids* 1994;42(11):1743–66.
- [6] Finnegan K, Kooistra G, Wadley HNG, Deshpande VS. The compressive response of carbon fiber composite pyramidal truss sandwich cores. In *J Mater Res* 2007;98(12):1264–72.
- [7] Kazemahvazi S, Tanner D, Zenkert D. Corrugated all-composite sandwich structures. Part 2: Failure mechanisms and experimental programme. *Comp Sci Technol* 2009;69(7–8):920–5.
- [8] Russell BP, Deshpande VS, Wadley HNG. Quasistatic deformation and failure modes of composite square honeycombs. *J Mech Struct* 2008;3(7):1315–40.
- [9] Radford DD, McShane GJ, Deshpande VS, Fleck NA. Dynamic compressive response of stainless-steel square honeycombs. *J Appl Mech* 2007;74(4):658–67.
- [10] Tilbrook MT, Radford DD, Deshpande VS, Fleck NA. Dynamic crushing of sandwich panels with prismatic lattice cores. *Int J Solid Struct* 2007;44(18–19):6101–23.
- [11] Russell BP, Malcolm A, Wadley HNG, Deshpande VS. Dynamic compressive response of composite corrugated cores. *J Mech Mater Struct* 2010;5(3):477–93.
- [12] Fleck NA, Deshpande VS. The resistance of clamped sandwich beams to shock loading. *J Appl Mech* 2004;71(3):286–401.
- [13] Xue Z, Hutchinson JW. A comparative study of blast-resistant metal sandwich plates. *Int J Impact Eng* 2004;30(10):1283–305.
- [14] Fleck NA. Compressive failure of fibre composites. *Adv Appl Mech* 1997;33:43–119.
- [15] Jelf PM, Fleck NA. The failure of composite tubes due to combined compression and torsion. *J Mater Sci* 1994;29:3080–4.
- [16] Mouritz AP, Bannister MK, Falzon PJ, Leong KH. Review of applications for advanced three-dimensional fibre textile composites. *Compos Part A – Appl S* 1999;30(12):1445–61.